A theory of mechanical stress-induced H2O2 signaling waveforms in Planta

Citation: Journal of Mathematical Biology. 2022 Dec 07;86(1):11

As Published: https://doi.org/10.1007/s00285-022-01835-y

Publisher: Springer Berlin Heidelberg

Persistent URL: https://hdl.handle.net/1721.1/146798

Version: Author's final manuscript: final author's manuscript post peer review, without publisher's formatting or copy editing

A theory of mechanical stress-induced H2O2 signaling waveforms in Planta

A Theory of Mechanical Stress-Induced H_2O_2 Signaling Waveforms *in Planta*[#]

Thomas K. Porter[1], *Michael N. Heinz*[2], *Daniel James Lundberg*[1], *Allan M. Brooks*[1], *Tedrick Thomas Salim Lew*[1,3], *Kevin S. Silmore*[1], *Volodymyr B. Koman*[1], *Mervin Chun-Yi Ang*[4], *Duc Thinh Khong*[4], *Gajendra Pratap Singh*[4], *James W. Swan*[1,†], *Rajani Sarojam*[4,5], *Nam-Hai Chua*[4,5] *and Michael S. Strano*[1*]

[1]Department of Chemical Engineering, Massachusetts Institute of Technology, Cambridge, MA 02139.

[2]Department of Mathematics, University of California, Berkeley, CA 94720.

[3]Institute of Materials Research and Engineering, Agency for Science, Technology and Research (A*STAR), Singapore 138634.

[4]Disruptive & Sustainable Technologies for Agricultural Precision IRG, Singapore-MIT Alliance for Research and Technology, 1 CREATE Way, #03-06/07/08 Research Wing, Singapore 138602, Singapore

[5]Temasek Life Sciences Laboratory Limited, 1 Research Link National University of Singapore, Singapore 117604, Singapore

[†] Deceased

*Corresponding author: strano@mit.edu

[#]This paper is dedicated, with appreciation, to our colleague and co-author Professor James W. Swan, who died suddenly on Nov. 5th, 2021.

Abstract

Recent progress in nanotechnology-enabled sensors that can be placed inside of living plants has shown that it is possible to relay and record real-time chemical signaling stimulated by various abiotic and biotic stresses. The mathematical form of the resulting local reactive oxygen species (ROS) wave released upon mechanical perturbation of plant leaves appears to be conserved across a large number of species, and produces a distinct waveform from other stresses including light, heat and pathogen-associated molecular pattern (PAMP)-induced stresses. Herein, we develop a quantitative theory of the local ROS signaling waveform resulting from mechanical stress in planta. We show that nonlinear, autocatalytic production and Fickian diffusion of H_2O_2 followed by first order decay well describes the spatial and temporal properties of the waveform. The reaction-diffusion system is analyzed in terms of a new approximate solution that we introduce for such problems based on a single term logistic function ansatz. The theory is able to describe experimental ROS waveforms and degradation dynamics such that species-dependent dimensionless wave velocities are revealed, corresponding to subtle changes in higher moments of the waveform through an apparently conserved signaling mechanism overall. This theory has utility in potentially decoding other stress signaling waveforms for light, heat and PAMP-induced stresses that are similarly under investigation. The approximate solution may also find use in applied agricultural sensing, facilitating the connection between measured waveform and plant physiology.

Keywords

- Plant Systemic Stress Signaling
- Plant Wounding Response
- ROS Wave
- Reaction-Diffusion
- Solitons

1. Introduction

As sessile organisms lacking mobile immune cells (Han, 2019), plants must quickly activate acclimation and defense responses to abiotic and biotic stresses via rapid cell-to-cell signaling (Fichman and Mittler, 2020). Such rapid cell-to-cell signaling is interdependently mediated by the ROS wave, Ca^{2+} wave, electrical signaling, and hydraulic signaling (Choi et al., 2017; Gilroy et al., 2014; Johns et al., 2021; Vega-

Muñoz et al., 2020). These signals are intricately linked to the production of phytohormones, such as salicylic acid, jasmonates, abscisic acid, ethylene, and auxins, which are involved in mediating adaptive responses to abiotic and biotic stresses (Navarro et al., 2006; Pieterse et al., 2012; Spoel and Dong, 2008; Truman et al., 2007). Recently, we demonstrated the use of single-walled carbon nanotube (SWNT) optical sensors in plant leaves to measure the spatial and temporal dynamics of the local ROS wave in real-time in response to mechanical wounding, heat, light, and pathogen-associated molecular pattern (PAMP)-induced stresses (Lew et al., 2020). We found that a characteristic mechanical wounding-induced ROS waveform was produced in six different species, and this waveform was distinct from heat, light, and PAMP-induced ROS waveforms. In order to better understand the differences between these waveforms, the possible specificity encoded within the ROS waveforms for different stresses, and the integration of the ROS wave with other signaling pathways, a mathematical theory describing these ROS waveforms is crucial. Herein, we develop a reaction-diffusion model based on a system of partial differential equations (PDEs) to describe the mechanical wounding ROS waveform and develop a single term logistic function ansatz as an approximate solution. This analytic description of the mechanical wound-induced ROS waveform provides a simple means for analyzing experimentally measured ROS waveforms across a wide-range of plant species.

ROS are a key class of molecules known to play an integral role in mediating the complex signaling pathways involved in abiotic and biotic stress responses (Fichman and Mittler, 2020). During normal plant growth, ROS, such as singlet oxygen, superoxide anions, hydroxyl radicals, and hydrogen peroxide (H_2O_2), are continuously produced as metabolic byproducts (Apel and Hirt, 2004; Petrov and Van Breusegem, 2012). ROS concentrations in subcellular compartments are tightly regulated by ROS scavengers, which include enzymes such as superoxide dismutase (SOD), catalase, ascorbate peroxidase, and glutathione peroxidase, and nonenzymatic antioxidants such as glutathione, ascorbic acid, flavonoids, tocopherol, alkaloids, and carotenoids (Apel and Hirt, 2004). Rapid and precise control of ROS levels is necessary, as ROS are involved in a host of signaling activities, such as cell cycle regulation, organogenesis, and stress

responses, including programmed cell death under very high concentrations (Huang et al., 2019; Van Breusegem et al., 2008).

When subjected to stress, plants rapidly produce ROS in a process known as oxidative burst. The primary source of this ROS is from plasma membrane-associated NADPH oxidases, or respiratory burst oxidase homologues (RBOHs). RBOHs catalyze the production of superoxide radicals, which are rapidly dismutated to H_2O_2 by SOD in the apoplast (Apel and Hirt, 2004; Gilroy et al., 2014; Huang et al., 2019; Johns et al., 2021; Mittler et al., 2011; Petrov and Van Breusegem, 2012). The initial oxidative burst triggers neighboring RBOHs into generating further oxidative bursts, resulting in an autocatalytic ROS wave that travels throughout the entire plant (Choi et al., 2017; Gilroy et al., 2014; Johns et al., 2021; Mittler et al., 2011; Petrov and Van Breusegem, 2012; Vega-Muñoz et al., 2020; Zandalinas and Mittler, 2018). Among ROS, H_2O_2 is of particular interest to researchers, as it has the longest half-life (~1 ms) and can traverse cell membranes via aquaporins, allowing it to travel long distances within the plant (Petrov and Van Breusegem, 2012). It is thus believed to be a key molecule in systemic responses such as systemic acquired resistance, systemic acquired acclimation, systemic wound responses, systemic metabolic responses, and systemic developmental responses (Gilroy et al., 2014).

Although it is evident that the ROS wave is a key component of early systemic stress responses, it remains unclear if and how this rapid signal encodes specific information, such as what kind of stress is being experienced (Apel and Hirt, 2004; Choi et al., 2017; Fichman and Mittler, 2020; Gilroy et al., 2014; Mittler et al., 2011). One way in which specificity could be encoded is in the spatial and temporal dynamics of the ROS wave (Choi et al., 2017; Fichman and Mittler, 2020; Mittler et al., 2011), which we have previously shown to vary among different stresses (Lew et al., 2020). In particular, the shape of the propagating wave, or the waveform, may contain valuable information on the production and degradation dynamics of H_2O_2, providing a link between H_2O_2 and its concurrent and downstream signaling pathways. Further, as Vestergaard et al. describe, the refractory time (i.e., the minimum time between the occurrence of discernible signaling events) of the signal is dependent on the rate of H_2O_2 degradation, which greatly

impacts how the H_2O_2 signal is perceived within the plant (Vestergaard et al., 2012). Thus, a mathematical description of the H_2O_2 waveform is highly desirable.

In prior work, we utilized SWNTs wrapped in single-stranded $(GT)_{15}$ oligonucleotides to monitor H_2O_2 stress-response signaling in plant leaves (Lew et al., 2020). The SWNTs primarily localized on plasma membranes and within chloroplasts in the epidermis and mesophyll layers, which is consistent with LEEP (lipid exchange envelope penetration) model predictions of nanoparticle localization based on size and zeta potential (Lew et al., 2018; Wong et al., 2016). This enabled detection of H_2O_2 signaling within the apoplast and chloroplasts during stress events. The SWNT sensor demonstrated high selectivity for H_2O_2 compared to other ROS and common plant analytes. We measured the local H_2O_2 waveform in six plant species: lettuce (*Lactuca sativa*), arugula (*Eruca sativa*), spinach (*Spinacia oleracea*), strawberry blite (*Blitum capitatum*), sorrel (*Rumex acetosa*), and *Arabidopsis thaliana*, and demonstrated a conserved wound-induced H_2O_2 signaling pathway in the defense responses of these different species (Lew et al., 2020). All waveforms were measured at organ-scale resolution within the stressed leaf at standoff distances. We hypothesized that the ROS waveform generated from mechanical wounding can be described by an autocatalytic wave propagation model. In the solution to this model, the concentration profile of H_2O_2 maintains a consistent traveling waveform for a given constant wave velocity. This type of solution is generally known as a soliton and commonly arises in nonlinear PDEs where dispersive effects balance nonlinear effects to yield a self-reinforcing traveling wave solution (Lomdahl, 1984). Because solitons arise from nonlinear systems, they do not obey the superposition principle, meaning that they preserve their speeds and waveforms upon collisions with other waves. The soliton description of the ROS wave thus captures the essential nature of autocatalytic ROS wave propagation and suggests a transport mechanism for systemic signaling (Mittler et al., 2011). In this work, we develop an approximate analytical solution to the governing PDEs describing our proposed model by implementing a change of variables that reduces the model to a system of ordinary differential equations (ODEs). In addition to providing a link for analyzing the ROS wave and concurrent and downstream signaling pathways, this analytic description may also serve

as a starting point for decoding signal specificity within the ROS wave and link measured waveform to plant physiology.

2. Model Formulation

We propose a one-dimensional reaction-diffusion model to describe ROS wave propagation (**Figure 1**). In our model, H_2O_2 (species A) freely diffuses with diffusion coefficient D and is autocatalytically produced with rate constant k upon reaction with an immobile (membrane-bound) precursor (species P) such as NADPH oxidase following the reaction

$$A + P \xrightarrow{k} A + A. \tag{1}$$

The conversion of superoxide radicals produced by NADPH oxidase to H_2O_2 via SODs is rapid (Klug et al., 1972) and thus neglected in our proposed model. We assume that H_2O_2 then degrades following first-order kinetics with rate constant k_d due to antioxidants within the plant:

$$A \xrightarrow{k_d} B. \tag{2}$$

Here, species B is a generic H_2O_2 degradation product. We assume that the concentration of precursor species P is initially spatially homogeneous and that P does not regenerate on the time scale of H_2O_2 wave propagation.

Both A and P vary spatially and temporally within the plant tissue, mapped by quantities specified as $A(z,t)$, $P(z,t)$, and $B(z,t)$. The corresponding mass balances of each species are then

$$\frac{\partial A}{\partial t} = D\frac{\partial^2 A}{\partial z^2} + kAP - k_d A, \tag{3}$$

$$\frac{\partial P}{\partial t} = -kAP, \tag{4}$$

$$\frac{\partial B}{\partial t} = k_d A, \tag{5}$$

with initial conditions

$$A(z, t = 0) = A_0(z), \tag{6}$$

$$P(z, t = 0) = P_0, \tag{7}$$

$$B(z, t = 0) = 0. \tag{8}$$

A_0 models the initial concentration of species A resulting from the ROS burst upon mechanical wounding at $z = 0$, and P_0 is the initial precursor concentration in the plant. Note that Equations 3 and 4 form a coupled set of PDEs, whereas Equation 5 can simply be integrated in time once A is found to solve for B.

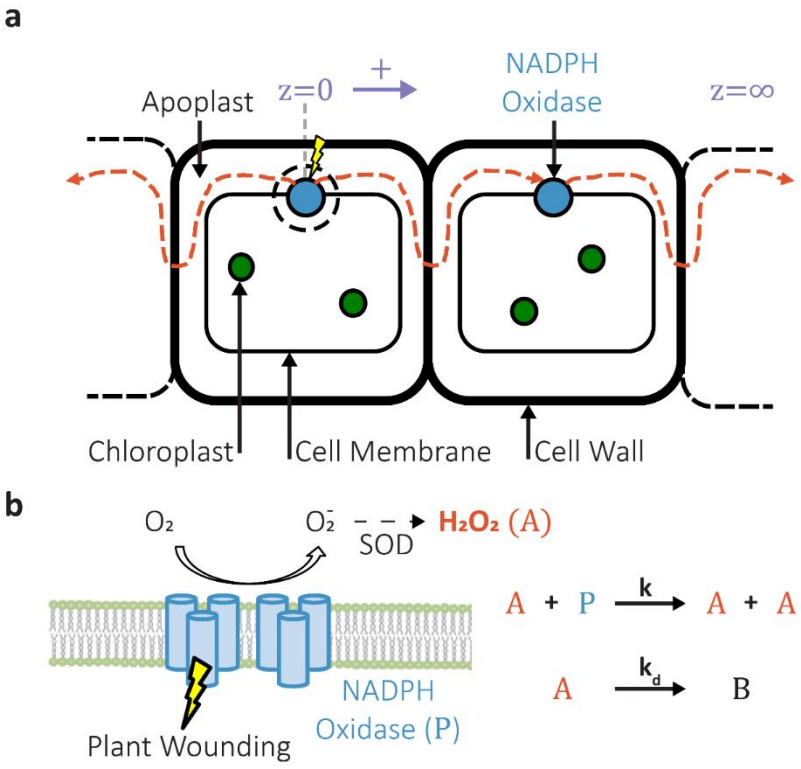

Figure 1. Schematic of ROS wave propagation model domain. a. H_2O_2 (red-orange dashed line) is autocatalytically generated by plasma membrane-localized NADPH oxidases (blue circles) and travels from cell to cell via the apoplast. Here, $z = 0$ marks the wounding location. **b.** Upon plant wounding, NADPH oxidases catalyze superoxide radical formation, and superoxide radicals are converted to H_2O_2 via

superoxide dismutases (SODs). The rapid conversion of superoxide radicals to H_2O_2 is neglected in our model, and H_2O_2 production is described by an overall reaction rate k. The H_2O_2 later degrades to species B following first order kinetics with rate k_d.

2.1 Non-Dimensionalization

It is useful to non-dimensionalize the above system of equations to facilitate numerical and analytical analysis. A dimensionless distance, x, and a dimensionless time, τ, are defined by scaling by a diffusion length, δ, and a diffusion timescale, t_c, respectively:

$$x = \frac{z}{\delta}, \qquad \delta = \sqrt{\frac{D}{kP_0}}, \tag{9}$$

$$\tau = \frac{t}{t_c}, \qquad t_c = \frac{\delta^2}{D} = \frac{1}{kP_0}. \tag{10}$$

The three concentrations are scaled in space and time and normalized by P_0:

$$\bar{A}(x,\tau) = \frac{A(z,t)}{P_0}, \qquad \bar{P}(x,\tau) = \frac{P(z,t)}{P_0}, \qquad \bar{B}(x,\tau) = \frac{B(z,t)}{P_0}. \tag{11}$$

The material balances become

$$\frac{\partial \bar{A}}{\partial \tau} = \frac{\partial^2 \bar{A}}{\partial x^2} + \bar{A}\bar{P} - \alpha \bar{A}, \tag{12}$$

$$\frac{\partial \bar{P}}{\partial \tau} = -\bar{A}\bar{P}, \tag{13}$$

$$\frac{\partial \bar{B}}{\partial \tau} = \alpha \bar{A}, \tag{14}$$

where the rate of H_2O_2 decay is scaled accordingly:

$$\alpha = \frac{k_d}{kP_0}. \tag{15}$$

Note that $\alpha \geq 0$. The initial conditions are also scaled accordingly:

$$\bar{A}(x, \tau = 0) = \bar{A}_0(x) = \frac{A_0(z)}{P_0}, \tag{16}$$

$$\bar{P}(x, \tau = 0) = 1, \tag{17}$$

$$\bar{B}(x, \tau = 0) = 0. \tag{18}$$

2.2 Translation to the Lagrangian Frame

Equations 3 and 4 and their non-dimensionalized forms from Equations 12 and 13 have been previously investigated to model the spatial spread of rabies among foxes (Källén et al., 1985). In this prior work, it was demonstrated that traveling wave solutions exist under certain conditions, as described below.

To look for traveling wave solutions, it is useful to move to a frame of reference relative to the wave itself, defined by $\eta = x - c\tau$. This enables us to seek a traveling wave solution of the form $\bar{A}(x, \tau) = f(x - c\tau) = f(\eta)$, $\bar{P}(x, \tau) = g(x - c\tau) = g(\eta)$, and $\bar{B}(x, \tau) = h(x - c\tau) = h(\eta)$. Here, c is the constant wave speed of the traveling wave solution. This transforms Equations 12-14 into the system of ODEs

$$-cf' = f'' + fg - \alpha f, \tag{19}$$

$$cg' = fg, \tag{20}$$

$$ch' = -\alpha f, \tag{21}$$

with boundary conditions

$$f(\pm\infty) = 0, \qquad g(\infty) = 1, \qquad h(\infty) = 0. \tag{22}$$

Again, note that Equations 19 and 20 form a coupled set of ODEs, whereas Equation 21 can simply be integrated once f is found to solve for h.

We look for traveling wave solutions which are bounded and positive in $(-\infty, \infty)$. When $0 \leq \alpha < 1$, Källén proved that such solutions exist for f and g, governed by the system of ODEs given by Equations

19 and 20 (Källén, 1984). In the boundary case of $\alpha = 0$, the boundary conditions are slightly different since H_2O_2 does not degrade (see Equation 40 in Section 3.1). When $\alpha > 1$, which is equivalent to $k_d > kP_0$, H_2O_2 decays faster than it is produced and a wave cannot persist. When $\alpha = 1$, which is equivalent to $k_d = kP_0$, H_2O_2 decays at the same rate at which it is produced, so any traveling wave solution for A would have to be constant. To satisfy the boundary conditions, A must be uniformly zero, meaning that a positive traveling wave solution does not exist. A more detailed analysis and proof that the traveling wave solutions exist if and only if $\alpha < 1$ was demonstrated by Källén (Källén, 1984). The remainder of this work will focus exclusively on $\alpha \in [0,1)$.

Since f and g are positive everywhere, it is clear from Equation 20 that g is increasing. This means that the limit $g(-\infty) = \gamma_g$ exists and satisfies $0 \leq \gamma_g < 1$, and that $\gamma_g < g(\eta) < 1$ for all η. It can further be shown that $\gamma_g = 0$ when $\alpha = 0$ and $\gamma_g > 0$ when $0 < \alpha < 1$ (see **Supplementary Information** for details).

To see the existence of a positive and bounded solution to Equation 21 for h when $0 < \alpha < 1$, we rearrange Equations 20 and 21:

$$f = \frac{c}{g} g' = -\frac{c}{\alpha} h'. \tag{23}$$

Integrating Equation 23 and evaluating the integration constant to be 0 from the boundary conditions at $\eta \to \infty$ yields a relationship between h and g:

$$h = -\alpha \ln g\,. \tag{24}$$

h is thus positive and bounded, since $0 < \gamma_g < g < 1$, proving the existence of the desired traveling wave solution. Additionally, one can use Equation 24 with Equation 29 from Section 2.3 to derive that $h(-\infty) = 1 - \gamma_g$.

The above boundary conditions indicate that there is no f before and after the reaction wave occurs ($\eta \to \pm\infty$). $\gamma_g \in (0,1)$ represents a constant residual amount of g that remains unconsumed after the wave has passed ($\eta \to -\infty$). When the degradation parameter α is low, f continues to react with g until g is (nearly) completely consumed. γ_g becomes larger with increasing α, as f is rapidly consumed without completely reacting all g. There is no h present before the reaction wave. Any f that was produced during the wave is eventually converted to h, yielding the value for $h(-\infty)$.

It can also be shown that the concentration profiles do not change before and after the wave has passed for all species (see **Supplementary Information** for details):

$$f'(\pm\infty) = g'(\pm\infty) = h'(\pm\infty) = 0. \tag{25}$$

We note that the equations do not have unique solutions based on our boundary conditions at $\eta \to \pm\infty$, as the traveling wave solutions translate along η arbitrarily. In this work, we find an approximate solution to Equations 19-21 which describes the shape of the waveform, and we utilize the translational invariance of the waveform to compare numerical and approximate solutions.

2.3 Stability Analysis

The case of stable wave generation has been considered previously for the system of PDEs from Equations 12-13 and the corresponding system of ODEs from Equations 19-20. Several researchers have derived stability criteria for the resulting propagating waves by analyzing linear stability about fixed points (Källén, 1984; Källén et al., 1985; Kot, 2001). Their analysis is recapped here for $0 < \alpha < 1$. First, the fixed points of the system are identified. Plugging in the expression for f in terms of g and g' from Equation 23 into Equation 19 yields

$$-cf' = f'' + cg' - \frac{\alpha c}{g} g' = f'' + cg' - \alpha c(\ln g)'. \tag{26}$$

Integrating and evaluating the $\eta \to \infty$ limit (before the wave) yields an integration constant equal to c:

$$c = f' + cf + cg - \alpha c \ln g\,. \tag{27}$$

Next, evaluating the $\eta \to -\infty$ limit (after the wave has passed) yields

$$c = c\gamma_g - \alpha c \ln \gamma_g\,. \tag{28}$$

Equation 28 can be simplified to yield an expression for α in terms of γ_g, which can be used to solve for γ_g:

$$\alpha = \frac{\gamma_g - 1}{\ln \gamma_g} = \frac{k_d}{kP_0}. \tag{29}$$

Next, Equations 20 and 27 are rearranged:

$$g' = \frac{1}{c} f g, \tag{30}$$

$$f' = c(1 + \alpha \ln g - f - g). \tag{31}$$

From Equation 30, the zero-growth isoclines for g are found by setting $g' = 0$ and are given by $g = 0$ and $f = 0$. Similarly, from Equation 31, the zero-growth isocline for f is given by

$$f = \alpha \ln g - g + 1. \tag{32}$$

From the phase plane, the fixed points $(g, f) = (1, 0)$ and $(\gamma_g, 0)$ can be identified from the intersections of the zero-growth isoclines for f and g (**Figure 2a**). These correspond to the pre-wave and post-wave equilibria. The Jacobian matrix for Equations 30 and 31 is

$$\boldsymbol{J} = \begin{bmatrix} \frac{f}{c} & \frac{g}{c} \\ -c + \frac{\alpha c}{g} & -c \end{bmatrix}. \tag{33}$$

Plugging in the fixed point $(\gamma_g, 0)$ into Equation 33 and solving for the eigenvalues yields

$$\lambda = \frac{-c \pm \sqrt{c^2 - 4(\gamma_g - \alpha)}}{2}. \tag{34}$$

This corresponds to a saddle point, as the eigenvalues are real and have opposite signs (since $\gamma_g < \alpha$, see **Supplementary Information** for details). Similarly, plugging in the fixed point $(1, 0)$ into Equation 33 and solving for the eigenvalues yields

$$\lambda = \frac{-c \pm \sqrt{c^2 - 4(1 - \alpha)}}{2}. \tag{35}$$

When $c < 2\sqrt{1-\alpha}$, the fixed point is a stable focus because the eigenvalues are complex with negative real parts. When $c \geq 2\sqrt{1-\alpha}$, the fixed point is a stable node because the eigenvalues are real and negative. A heteroclinic connection cannot be made between the saddle point and stable focus without having an unphysical negative concentration of f (for example, **Figure 2b**). However, a positive heteroclinic connection can be made between the saddle point and stable node (for example, **Figure 2c**). Therefore, the minimum wave speed is governed by

$$c \geq 2\sqrt{1-\alpha}. \tag{36}$$

A similar analysis can be conducted to show that Equation 36 also holds for $\alpha = 0$ (see **Supplementary Information** and **Figure S1** for details).

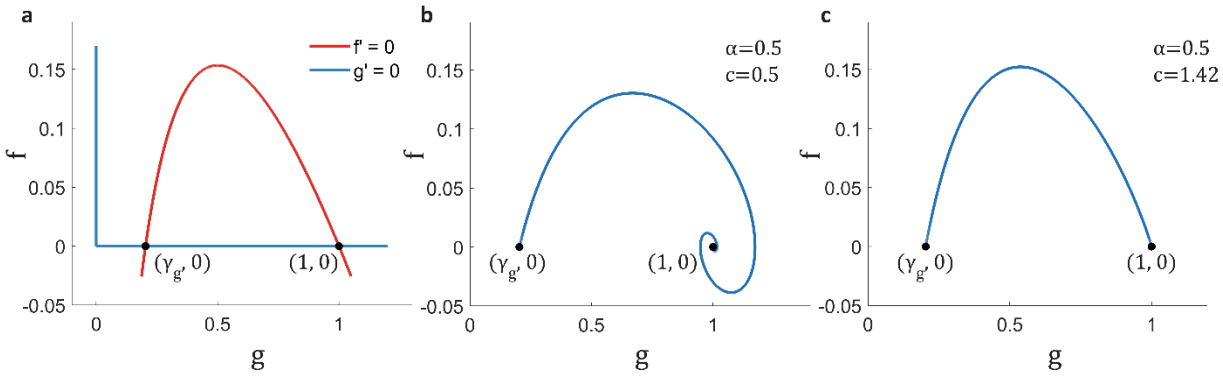

Figure 2. Phase portraits illustrating minimum wave speed requirement for a traveling wave solution for $0 < \alpha < 1$. a. The zero-growth isoclines for f and g from setting Equations 30 and 31 equal to zero. The marked points denote the two equilibria $(g, f) = (1, 0)$ and $(\gamma_g, 0)$, before and after the wave, respectively. **b.** When the wave speed c is below the minimum possible value for a given dimensionless degradation rate parameter α, as determined by the equality in Equation 36, the saddle-focus connection implies unphysical negative concentrations of f. **c.** When the wave speed satisfies Equation 36, the saddle-node connection is positive.

2.4 Numerical Simulation

Equations 12-14 were numerically simulated in MATLAB using method of lines, where spatial derivatives were approximated using finite volume method (with cell width 0.004), and the adaptive stiff ODE solver *ode15s* was used to integrate in time. In addition to the initial conditions given by Equations 16-18, the following boundary conditions were employed:

$$\frac{\partial \bar{A}}{\partial x}(x = 0, \tau) = 0, \tag{37}$$

$$\bar{A}(x = L, \tau) = 0, \tag{38}$$

where $[0, L]$ is the specified spatial domain. These boundary conditions represent no flux from the left boundary and a concentration of zero for species $\bar{A}$ at the right boundary, as L is set large enough that the wave never touches the right boundary. The initial condition $\bar{A}_0(x)$ resulting from the ROS burst upon mechanical wounding (Equation 16) was modeled by setting $\bar{A} = 10^{-3}$ in the cell at $x = 0$, and setting $\bar{A} = 0$ otherwise for $\tau = 0$.

We observed the minimum possible wave speed governed by the equality in Equation 36 in our numerical simulations of the PDEs (Equations 12-14) for sharp initial disturbances (**Figure 3a-b**), as expected (Källén, 1984). Indeed, Källén proved that if the initial condition $\bar{A}(x, \tau = 0) = \bar{A}_0(x)$ for the PDE has bounded support and the solution $\bar{A}(x, \tau)$ takes the form of a travelling wave for large τ, then the travelling wave

must travel with the minimum speed $c = 2\sqrt{1-\alpha}$. This information was used when converting to dimensional form for comparison to experimental data (see Section 3.3). In this work, we develop approximate analytical solutions to the model PDE system (converted to an ODE system via change of variables) for constant wave speeds, using the positive minimum wave speed $c = 2\sqrt{1-\alpha}$.

For fitting to experimental concentration versus time data (Section 3.3), α was used as a fitting parameter. When comparing numerical simulations with experimental data and analytical approximations, fully developed waveforms from numerical simulations were used (i.e., $\bar{A}$, $\bar{P}$, and $\bar{B}$ versus τ were selected for a specific value of x such that the imposed boundary conditions in x did not confound the simulated wave profile). We chose $\bar{A}\left(x=\frac{L}{2},\tau\right)$, $\bar{P}\left(x=\frac{L}{2},\tau\right)$, and $\bar{B}\left(x=\frac{L}{2},\tau\right)$ for all comparisons of numerical simulations with experimental data and analytical approximations (see example waveforms in **Figure 3c-f**).

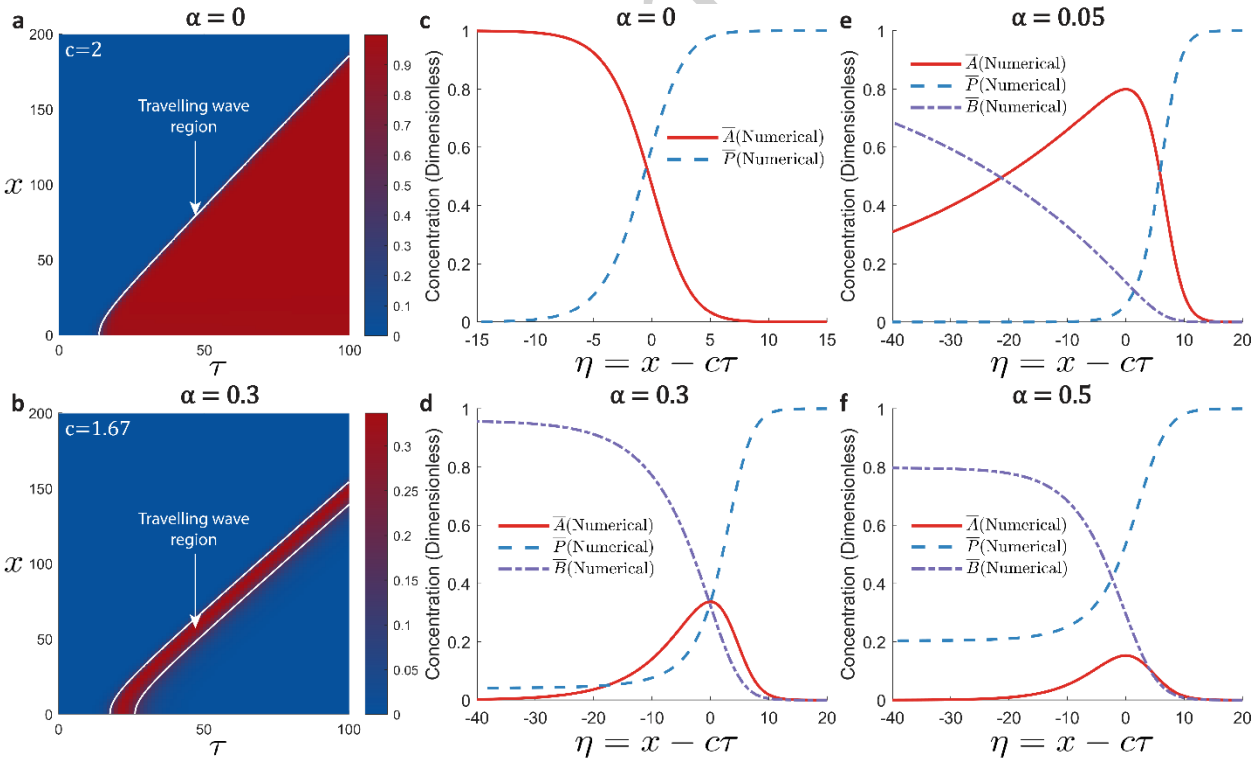

Figure 3. Numerically simulated traveling wave solutions to the governing PDEs. Numerical simulations of Equations 12-14 using initial conditions from Equations 16-18 and boundary conditions from Equations 37 and 38 for a few different values of the dimensionless degradation rate α. **a, b.** 2-dimensional projections of $\bar{A}(x,\tau)$ for $\alpha = 0$ and $\alpha = 0.3$. The white lines highlight the contour lines at half of the amplitude. Away from the $x = 0$ boundary, the wave travels at speed c governed by the equality in Equation 36, as demonstrated by the slope of the traveling wave region. **c-f.** Representative fully developed waveforms obtained from $\bar{A}\left(x = \frac{L}{2}, \tau\right)$, $\bar{P}\left(x = \frac{L}{2}, \tau\right)$, and $\bar{B}\left(x = \frac{L}{2}, \tau\right)$ were plotted as a function of $\eta = x - c\tau$, illustrating the distinct waveforms that arise for different values of α.

3. Development of Approximate Analytical Solution

A central question of this work is how the underlying H_2O_2 waveform in different plant species resulting from mechanical stress differs in subtle aspects, including the second moment of the asymmetric peak, despite being the product of H_2O_2 reaction and diffusion from a conserved biochemical stress signaling mechanism. Hence, an analytical solution can link the functional description of the waveform to underlying biochemical parameters that may vary from plant to plant.

We analyze two cases: one in which f does not degrade ($\alpha = 0$), and also the full system of equations ($0 < \alpha < 1$). The former case should be testable by using plant mutations which limit or exclude the production of catalases or certain peroxidases in the plant. The latter case applies to observed signaling waveforms in wildtype plants, according to the experimental results reported in Lew et al. (Lew et al., 2020).

We propose that an approximate solution can be derived starting from a single term logistic function with two or three parameters for the $\alpha = 0$ and $0 < \alpha < 1$ cases, respectively. The logistic function has been shown to be useful in the construction of exact solutions for many nonlinear PDEs (Kudryashov, 2015). These solutions are constructed by taking the nonlinear ODE obtained from the original PDE and comparing the form of the ODE with "standard" nonlinear differential equations derived from the Riccati equation ($y' = \theta_2 y^2 + \theta_1 y + \theta_0$, where θ_2, θ_1, and θ_0 are arbitrary constants) with known solutions in the form of

logistic functions. More recently, an ansatz of the form $w(\eta) = \sum_{i=0}^{N} \theta_i z^i(\eta)$ with constants θ_i and $z^i(\eta)$ as powers of a generalized logistic function has been successfully applied in constructing exact solutions to the dual-mode nonlinear Schrödinger's equation with Kerr law and dual power law nonlinearities (Pinar et al., 2020). Thus, the logistic function and its generalizations have great utility as tools for solving some nonlinear PDEs. Here, we take an approach similar to that of Abrahamson et al., in which we construct an approximate solution starting from a single term logistic function (Abrahamson and Strano, 2010). For the two-parameter logistic function, we employ the functional form

$$u(\eta) = (1 + Q_0 e^{s_0 \eta})^{-1/Q_0}. \tag{39}$$

Q_0 is a parameter that affects the position of the logistic curve along the η axis and its asymmetry, and s_0 is a parameter that affects the direction and growth rate of the logistic curve (**Figure 4**). The third parameter in the $0 < \alpha < 1$ case is more intuitive and described in Section 3.2. Because derivatives of the starting logistic function can be evaluated analytically, derived relationships between the coupled concentration species can be utilized to formulate closed-form functional solutions for all concentration profiles. This method is in part motivated by its simplicity and ease of application for the broader research community. The validity of our approximations is confirmed by agreement with numerical solutions.

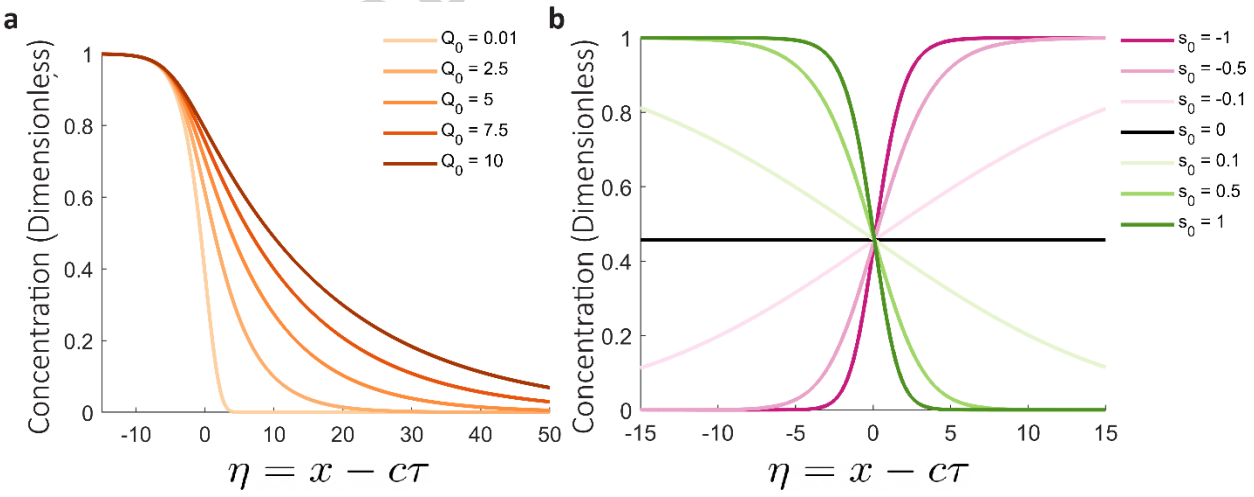

Figure 4. Effects of changing logistic function parameters (Equation 39). a. As Q_0 increases, the logistic curve becomes more asymmetric. The characteristic logistic curve shape is lost when $Q_0 \leq 0$, and is therefore not plotted here. In this plot, s_0 is fixed at 0.4907, the value from the $\alpha = 0$ case in Section 3.1. **b.** s_0 affects the direction and growth rate of the curve. Note that the curves are not symmetric about their midpoints. In this plot, Q_0 is fixed at 0.6006, the value from the $\alpha = 0$ case in Section 3.1.

3.1 $\alpha = 0$

First, we consider the simplified case in which there is no degradation of f (i.e., $\alpha = 0$, $c = 2$). We focus on f and g (Equations 19 (with $\alpha = 0$) and 20), as h is never produced in this scenario.

The boundary conditions are slightly different than previously described in Equation 22:

$$f(-\infty) = 1, \qquad f(\infty) = 0, \qquad g(\infty) = 1. \tag{40}$$

As discussed in Section 2.2, the limit $g(-\infty) = \gamma_g$ exists and equals 0 in this case. These boundary conditions indicate that there is no f before the reaction wave occurs ($\eta \to \infty$). After the wave has passed ($\eta \to -\infty$), all g has been converted into f.

Again, it can be shown that the concentration profiles do not change before and after the wave has passed for all species (see **Supplementary Information** for details):

$$f'(\pm\infty) = g'(\pm\infty) = 0. \tag{41}$$

A combined overall mass balance can be derived by plugging Equation 20 into Equation 19 with $\alpha = 0$:

$$-cf' = f'' + cg'. \tag{42}$$

Another useful expression can be derived by integrating Equation 42 and evaluating the limit as $\eta \to \infty$, which yields an integration constant equal to $-c$:

$$-cf = f' + cg - c. \tag{43}$$

Rearranging this equation yields a relationship between f and g:

$$g = \frac{c - cf - f'}{c}. \tag{44}$$

With guidance from the numerical solution (**Figure 3**), we seek solutions to the coupled ODEs starting from a two-parameter logistic function description of f:

$$f(\eta) = (1 + Q_0 e^{s_0 \eta})^{-1/Q_0}, \tag{45}$$

with parameters Q_0 and s_0 as described earlier (**Figure 4**). From Equation 44, a functional form for g may then be derived:

$$g(\eta) = 1 + \frac{-c + (s_0 - cQ_0)e^{s_0 \eta}}{c(1 + Q_0 e^{s_0 \eta})^{\,1+1/Q_0}}. \tag{46}$$

With these functional descriptions of f and g, we next seek to derive self-consistent expressions to describe the parameters Q_0 and s_0. Specifically, we choose to derive expressions that exactly satisfy Equations 19 and 20 at the points $\eta = 0$ and $\eta = \frac{1}{s_0}$. In doing so, we assume that the parameters Q_0 and s_0 may be approximated as constants independent of η. These points were selected to be in the dynamic region of the wave (in between the boundary condition values) and to yield relatively simple expressions. This assumption is later validated by the agreement of the analytical approximations to the numerical solutions.

Plugging in the functional forms (Equations 45 and 46) into the governing equation for f (Equation 19) and evaluating at $\eta = 0$ and $\eta = \frac{1}{s_0}$ yields the following equations, respectively:

$$s_0 = \frac{c(1 + Q_0) + c(1 + Q_0)^{1/Q_0}(-1 - Q_0)}{1 - c^2(1 + Q_0)^{1/Q_0}}, \tag{47}$$

$$1 - \frac{cs_0 e}{1 + Q_0 e} + \frac{s_0^2 e(-1 + e)}{(1 + Q_0 e)^2} - \frac{c + cQ_0 e - s_0 e}{c(1 + Q_0 e)^{\,1+\frac{1}{Q_0}}} = 0. \tag{48}$$

Equations 47 and 48 can be solved simultaneously to yield parameter values $Q_0 = 0.6006$ and $s_0 = 0.4907$. The functional forms demonstrate agreement with the numerical solution (**Figure 5**):

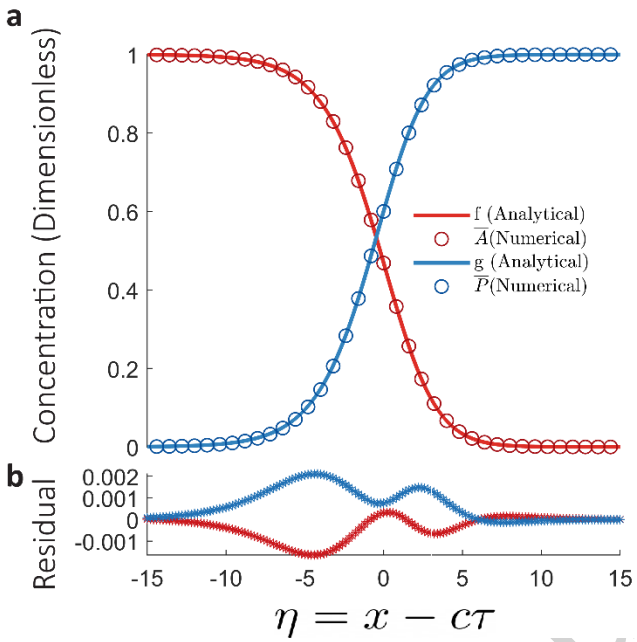

Figure 5. Comparison of analytical approximation to numerical simulation for $\alpha = 0$ (no decay of H_2O_2). Analytical approximations were derived starting from a two-parameter logistic function description of f (H_2O_2). **a.** Analytical approximations (solid lines; Equations 45 and 46, with parameter values $Q_0 = 0.6006$ and $s_0 = 0.4907$ described by Equations 47 and 48, and $c = 2$ from the equality in Equation 36) are plotted with numerical solutions (circle markers; Equations 12 (with $\alpha = 0$) and 13, with initial conditions from Equations 16 and 17 and boundary conditions from Equations 37 and 38). **b.** The residuals for f and g (precursor species) compared to their corresponding numerical solutions, given by $f_{analytical} - \bar{A}_{numerical}$ (red) and $g_{analytical} - \bar{P}_{numerical}$ (blue), are plotted against η.

This description of the $\alpha = 0$ case provides a simple functional form that decouples H_2O_2 production dynamics from degradation dynamics, and may find use in the analysis of H_2O_2 waveforms measured in plant mutants with limited H_2O_2-degrading antioxidant capacity.

3.2 $0 < \alpha < 1$

We now consider the full system of ODEs, which includes the degradation of f, given by Equations 19-21 with boundary conditions as stated in Equation 22. Based on the boundary conditions, we note that the

profile of f can no longer be described by the same logistic function used in the $\alpha = 0$ case. Thus, a new approach must be taken. We first recall the expressions that link the concentration profiles of each species: f is related to g and h by Equation 23, and h and g are related by Equation 24. With guidance from the numerical solution (**Figure 3**), we seek solutions to the coupled ODEs starting from a three-parameter logistic function description of h, noting from Equation 24 that g is described as the log-logistic of h and from Equation 23 that f is described as the derivative of the logistic function describing h. From the post-wave ($\eta \to -\infty$) boundary conditions in Equation 22, we also see that the logistic expression for h must include an offset to account for the non-zero $\eta \to -\infty$ asymptote. This offset is captured in the third parameter $g(-\infty) = \gamma_g$. We thus seek solutions using the following functional forms:

$$h = \frac{\gamma_g - 1}{(1 + Qe^{s\eta})^{1/Q}} + 1 - \gamma_g, \tag{49}$$

$$g = exp\left[\frac{1}{\alpha}\left(\frac{1 - \gamma_g}{(1 + Qe^{s\eta})^{1/Q}} + \gamma_g - 1\right)\right], \tag{50}$$

$$f = \frac{cse^{s\eta}(\gamma_g - 1)(1 + Qe^{s\eta})^{-\frac{(1+Q)}{Q}}}{\alpha}. \tag{51}$$

The three parameters γ_g, Q, and s affect the shape of the waveform as described earlier (**Figure 4**) and are constant for a given wave speed (defined by α in Equation 36).

We next derive self-consistent expressions for each parameter to complete the description of the H_2O_2 wave described by the model for constant wave speeds. An expression for γ_g in terms of α was already derived and is given by Equation 29. For Q and s, we choose to derive expressions that exactly satisfy Equations 19-21 at the point $\eta = 0$. We again assume that these parameters are constants independent of η.

Equations 50 and 51 were directly plugged into Equation 19 and evaluated at $\eta = 0$, yielding an expression for s in terms of α, γ_g, and Q:

$$s = -\sqrt{(1+Q)\left(\gamma_g^{1-(1+Q)^{-\frac{1}{Q}}} - \alpha\right)}, \qquad \alpha < \gamma_g^{1-(1+Q)^{-\frac{1}{Q}}}. \tag{52}$$

Here, the inequality ensures that all parameters take on real values. The sign of Equation 52 was chosen with guidance from the numerical solutions (**Figures 3 and 4**), as we expect $s < 0$. Because both Q and s are unknown, one more equation is necessary to develop a complete description. This was derived by first plugging in Equations 20 and 21 into Equation 19:

$$-cf' = f'' + cg' + ch'. \tag{53}$$

Integrating and evaluating the $\eta \to \infty$ limit (before the wave) yields an integration constant equal to c:

$$c = f' + c(f + g + h). \tag{54}$$

Evaluating Equation 54 at $\eta = 0$, noting that $f'(0) = 0$, yields

$$f(0) + g(0) + h(0) = 1. \tag{55}$$

Plugging in Equations 49-51 into Equation 55 and simplifying yields

$$\gamma_g = \frac{\gamma_g - 1}{(1+Q)^{\frac{1}{Q}}}\left[\frac{cs}{\alpha(1+Q)} + 1\right] + \gamma_g^{1-(1+Q)^{-\frac{1}{Q}}}. \tag{56}$$

Equation 52 can be plugged into this expression to yield an expression for Q in terms of α and γ_g:

$$\gamma_g = \frac{\gamma_g - 1}{(1+Q)^{\frac{1}{Q}}}\left[\frac{-c\sqrt{(1+Q)\left(\gamma_g^{1-(1+Q)^{-\frac{1}{Q}}} - \alpha\right)}}{\alpha(1+Q)} + 1\right] + \gamma_g^{1-(1+Q)^{-\frac{1}{Q}}}, \qquad \alpha < \gamma_g^{1-(1+Q)^{-\frac{1}{Q}}}. \tag{57}$$

For a given $\alpha \in (0, 1)$, Equation 29 can be solved for γ_g, then Equation 57 can be solved for Q, and Equation 52 can be used to calculate s. The residual between our analytic description and numerical solution is plotted for the example case $\alpha = 0.3$ (**Figure 6**). Although not trivial, the residual between our

analytic description and numerical solution is of the same order as the residual between the model and experimental data shown in Section 3.3, indicating the suitability of our analytical approximation for describing experimental data. The analytic descriptions demonstrate agreement with the numerical solutions across a broad range of α values (**Figure 7**):

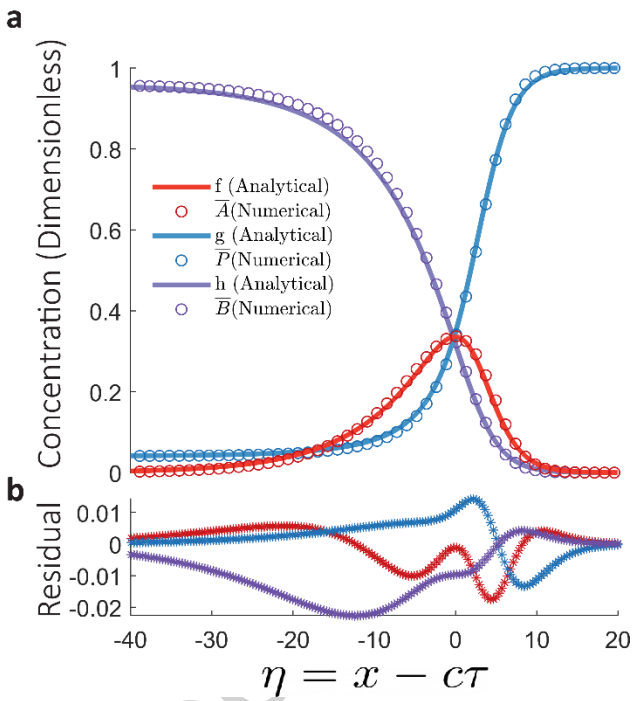

Figure 6. Comparison of analytical approximation to numerical simulation for $\alpha = 0.3$. Analytical approximations were derived starting from a three-parameter logistic function description of h (H_2O_2 degradation product) for $\alpha = 0.3$ as a sample case for the $0 < \alpha < 1$ solutions (where f (H_2O_2) degrades). **a.** Analytical approximations (solid lines; Equations 49-51, with parameter values $\gamma_g = 0.0409$, $Q = 3.9189$, and $s = -0.4638$ described by Equations 29, 52, and 57, and $c = 1.6733$ from the equality in Equation 36) are plotted with numerical solutions (circle markers; Equations 12-14, with initial conditions from Equations 16-18 and boundary conditions from Equations 37 and 38). **b.** The residuals for f, g (precursor species), and h compared to their corresponding numerical solutions, given by $f_{analytical} - \bar{A}_{numerical}$ (red), $g_{analytical} - \bar{P}_{numerical}$ (blue), and $h_{analytical} - \bar{B}_{numerical}$ (purple), are plotted against η.

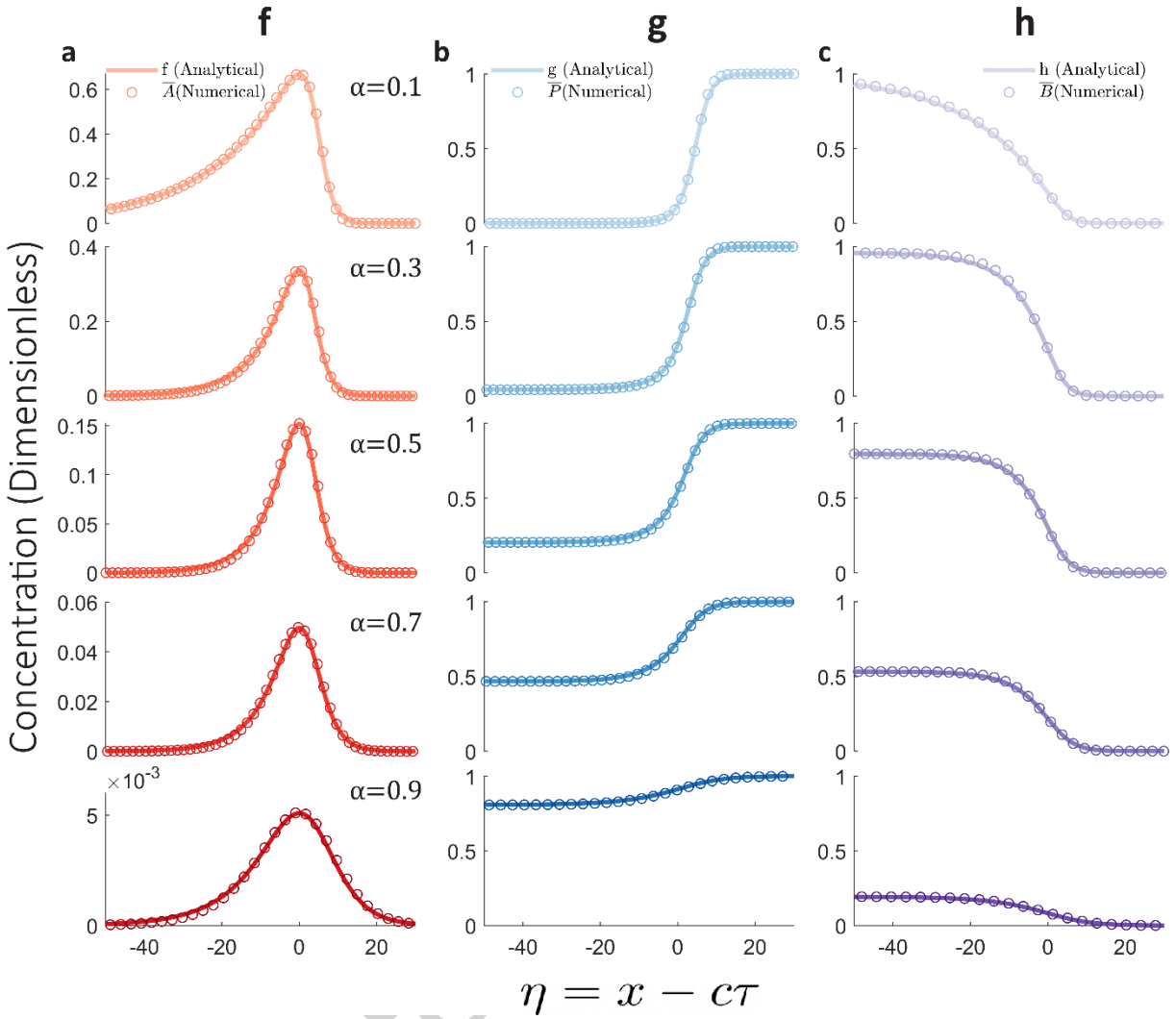

Figure 7. Comparison of analytical approximations to numerical simulations for $0 < \alpha < 1$. Analytical approximations (solid lines; Equations 49-51, with parameters γ_g, Q, and s described by Equations 29, 52, and 57, and c calculated from the equality in Equation 36) are plotted with numerical solutions (circle markers; Equations 12-14, with initial conditions from Equations 16-18 and boundary conditions from Equations 37 and 38) for varying dimensionless degradation rates (α) for **a.** f (H_2O_2 concentration), **b.** g (precursor concentration), and **c.** h (degradation product concentration) as a function of the traveling wave coordinate η. Analytical approximations were derived starting from a three-parameter logistic function to describe h. Darker hues correspond to higher α values.

We note that the solution becomes qualitatively inaccurate for very high (> 0.99) and very low (< 0.04) α values. In the case of low α, Equation 29 becomes difficult to solve numerically for γ_g, and the error propagates into the rest of the solution. The problem can be slightly mitigated by employing the variable transformation $\gamma_g = e^{\zeta}$, where $\zeta \in (-\infty, 0)$. Equation 29 is then rewritten as $\alpha = \frac{e^{\zeta}-1}{\zeta}$ and ζ can be solved to determine γ_g. The solution can then accurately describe concentration profiles down to $\alpha = 0.01$ and slightly lower. To our knowledge, this range of α values appears to be suitable for describing experimentally observed data. Our analytical approximation can be easily applied to analyze experimentally measured ROS waveforms in wildtype plants, as discussed in Section 3.3.

3.3 Application to Experimental Data

After deriving satisfactory approximate solutions to the governing system of ODEs, the functional descriptions must be transformed back into dimensional space to fit the model to experimental data. To achieve this, we consider a few key characteristics of the waveform shape: the amplitude, the full-width-at-half-maximum (FWHM), and the time at which the concentration reaches its maximum (**Figure 8a**). The amplitude is defined as the maximum concentration, and the FWHM is defined as the time between amplitude midpoints. To apply our model, we first tabulated parameter values for $0.01 \leq \alpha \leq 0.99$ in increments of 0.01 to generate solutions for a wide range of possible wave speeds (**Supplemental Data**). We then match the amplitude, FWHM, and peak location of the model solutions to the experimental data by vertical stretching, horizontal stretching, and horizontal translation. The stretching factors directly correspond to the scaling factors used for non-dimensionalizing the governing equations (Equations 9-11). The horizontal stretching factor is negative to account for the opposite signs of time and η.

The data in Lew et al., to the best of our knowledge, contains the only selective, high resolution measurements of the full endogenous H_2O_2 waveforms for different species and genetic mutants in the literature, made possible by the SWNT nanosensors (Lew et al., 2020). Using this data, we demonstrate that our model can successfully describe the local H_2O_2 waveform observed after mechanical wounding for

a variety of plant species (**Figure 8b-g,** data in **Supplemental Data**). When fitting the model to the data, we attempt to capture the most important features describing the shape of the asymmetric wave peak by selecting only the data points greater than or equal to 20% of the amplitude (light magenta data points in **Figure 8b-g**). In doing so, we avoid overfitting the model to the pre- and post-wave data. We find that changing this region of interest to select data points greater than or equal to 5-50% of the amplitude does not affect the results drastically (the best fit α parameter varies by 0.02 at most for the data shown in **Figure 8b-g**). To determine the best fit α value, we calculate the sum of least squares around the region of interest as described above for all tabulated model solutions for $0.01 \leq \alpha \leq 0.99$ and select the α value with the lowest sum. We find that the unique H_2O_2 waveforms observed in different plant species can be captured in our model by different values of α and dimensionless traveling wave velocities, which suggests that different plant species have different innate capacities for producing and degrading H_2O_2. We previously showed that these H_2O_2 wave velocities for each species are comparable to corresponding electrical signaling velocities for most species (Lew et al., 2020). Although the overall mechanical wound-induced H_2O_2 stress signaling mechanism appears to be conserved, there are subtle differences among different species that may be related to evolutionary adaptations of each species to their native environments (Ani Akpinar et al., 2012; Thaler et al., 2012).

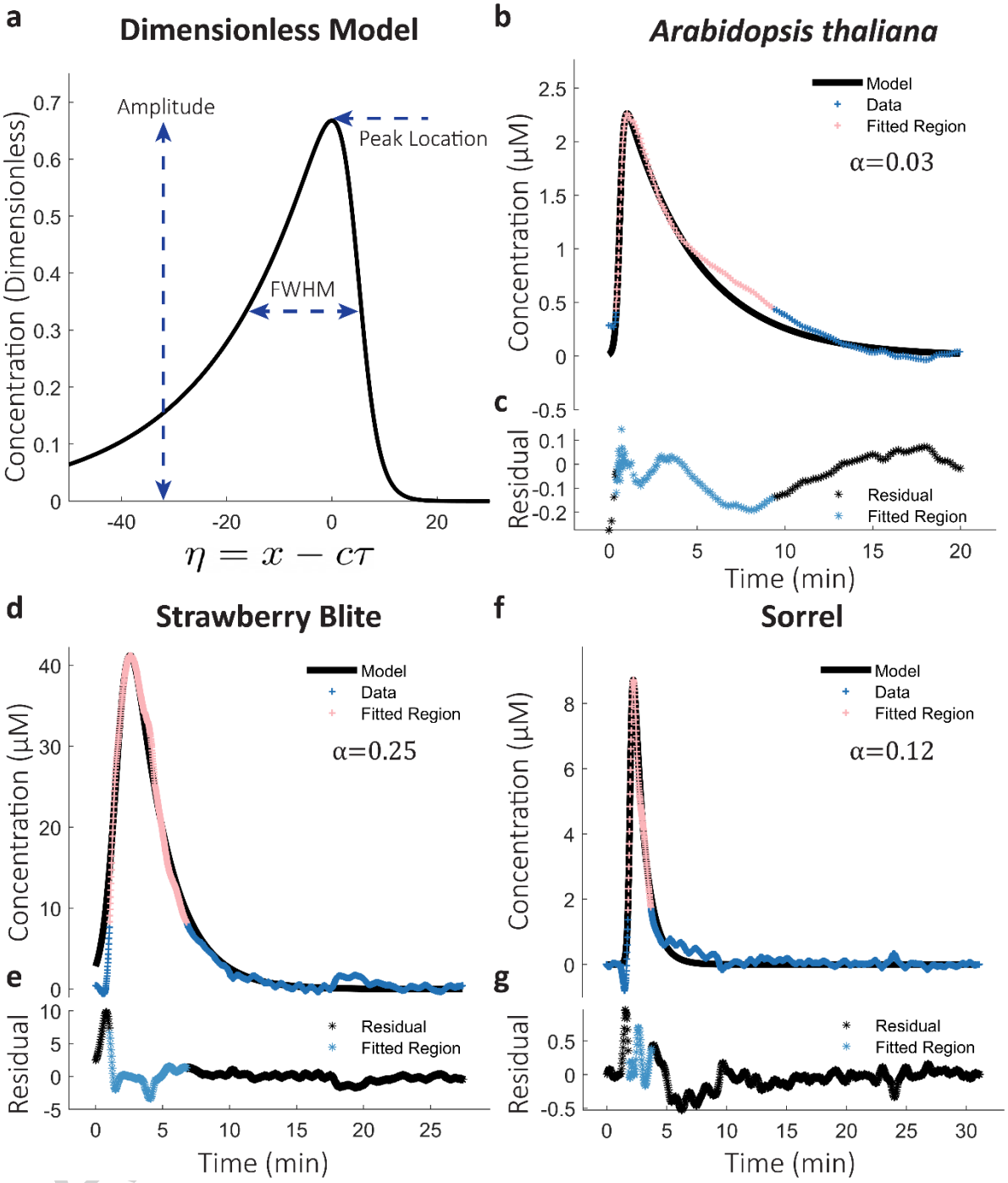

Figure 8. Model fitting to experimental data. Experimental data was collected in Lew et al. for H_2O_2 concentration in leaves after mechanical wounding with sharp forceps across the leaf midrib near the leaf tip at a fixed position in the leaf approximately 1 cm away from infiltrated sensors (Lew et al., 2020). $n = 8$ independent biological samples were measured for each species. **a.** The dimensionless model (Equation

51) was fit to experimental data by matching the amplitudes, full-widths-at-half-maximum (FWHM), and peak locations of the data. A horizontal reflection was also implemented to account for the opposite signs of time and η. α, the dimensionless degradation rate, was used as a fitting parameter. **b-g.** The model adequately describes the H_2O_2 waveform observed across several different species. We present a few representative cases here. Only the light magenta data points labeled "Fitted Region" were used for fitting the model. A residual plot of $[H_2O_2]_{analytical\ model} - [H_2O_2]_{experimental}$ is shown underneath each fit. The blue points in the residual plots correspond to the "Fitted Region" points. Different species appear to share a common wave signaling mechanism with differences in waveforms primarily captured by differences in the degradation rate α.

4. Conclusion

In this work, we have built upon our previously proposed reaction-diffusion model for mechanical wound-induced H_2O_2 stress signaling in plants by deriving an approximate analytical solution to the governing PDEs (converted to a system of ODEs via a change of variables). This solution yields a simple functional form to describe the local traveling H_2O_2 waveform at a given constant wave velocity. Our model describes the autocatalytic production of H_2O_2 with Fickian diffusion and first-order degradation. The precursor species is an immobile, membrane-bound protein such as NADPH oxidase. We non-dimensionalize the governing PDEs and convert them into ODEs using a traveling wave coordinate to combine space and time. We then employ a two or three parameter single term logistic function to describe one of the concentration profiles and derive relationships between each chemical species to develop functional form descriptions of them. We choose to satisfy the governing ODEs at specific points to derive equations for each parameter that can be solved self-consistently and validate our approach by comparison with numerical solutions. Finally, we apply the model to experimental data. We show that our model can be easily applied to experimental data and captures the essential features of the mechanical wound-induced H_2O_2 stress signaling waveform and its subtle differences among different plant species. The H_2O_2 wave signaling mechanism appears to be shared by different plant species, with differences in waveforms captured by

varying degradation rates (α) that correspond to varying wave velocities. Overall, our mathematical description of this waveform paves the way for linking systemic H_2O_2 stress signaling to its concurrent and downstream pathways, and can provide insights into the specificity that may be encoded within the H_2O_2 stress signal.

CRediT Authorship Contribution Statement

TKP: Data Curation, Formal analysis, Methodology, Software, Visualization, Writing – Original Draft (main text), Writing – Review & Editing. **MNH:** Formal analysis, Methodology, Software, Writing – Original Draft (Supplementary Information), Writing – Review & Editing. **DJL:** Formal analysis, Methodology, Writing – Review & Editing. **AMB:** Formal analysis, Methodology, Writing – Review & Editing. **TTSL:** Data Curation, Formal analysis, Investigation, Methodology, Software, Writing – Review & Editing. **KSS:** Formal analysis, Methodology, Software, Writing – Review & Editing. **VBK:** Formal analysis, Methodology, Writing – Review & Editing. **MCYA:** Investigation, Validation, Writing – Review & Editing. **DTK:** Investigation, Validation, Writing – Review & Editing. **GPS:** Conceptualization, Funding acquisition, Supervision, Writing – Review & Editing. **JWS:** Conceptualization, Formal analysis, Methodology, Supervision. **RS:** Conceptualization, Funding acquisition, Supervision, Writing – Reviewing & Editing. **NHC:** Conceptualization, Funding acquisition, Supervision, Writing – Review & Editing. **MSS:** Conceptualization, Formal analysis, Funding acquisition, Methodology, Supervision, Writing – Review & Editing.

Declaration of Competing Interest

The authors declare that they have no known competing financial interests or personal relationships that could have appeared to influence the work reported in this paper.

Acknowledgements

The mathematical and analytical work is supported by Nanotechnology for Agricultural and Food Systems (A1511) [grant no. 2021-67021-33999/project accession no. 1025638] from the USDA National

Institute of Food and Agriculture. The extension of the theory to plant signaling data was supported by the National Research Foundation (NRF), Prime Minister's Office, Singapore under its Campus for Research Excellence and Technological Enterprise (CREATE) program. The Disruptive & Sustainable Technology for Agricultural Precision (DiSTAP) is an interdisciplinary research group of the Singapore MIT Alliance for Research and Technology (SMART) Centre. DJL and TKP are grateful for support from the National Science Foundation Graduate Research Fellowship Program under Grant No. 1745302. TTSL acknowledges a graduate fellowship by the Agency of Science, Research and Technology, Singapore. KSS was supported by the Department of Energy Computational Science Graduate Fellowship program under grant DE-FG02-97ER25308. Professor Per-Olof Persson is acknowledged for helpful insights during the development of the approximate solutions.

Data Availability Statement

All data generated or analyzed during this study are included in this published article and its supplementary information files.

References

Abrahamson, J.T., Strano, M.S., 2010. Analytical Solution to Coupled Chemical Reaction and Thermally Diffusing Systems: Applicability to Self-Propagating Thermopower Waves. J. Phys. Chem. Lett. 1, 3514–3519. https://doi.org/10.1021/JZ101381M

Ani Akpinar, B., Avsar, B., Lucas, S.J., Budak, H., 2012. Plant abiotic stress signaling. Plant Signal. Behav. 7, 1–6. https://doi.org/10.4161/PSB.21894

Apel, K., Hirt, H., 2004. REACTIVE OXYGEN SPECIES: Metabolism, Oxidative Stress, and Signal Transduction. Annu. Rev. Plant Biol. 55, 373–399. https://doi.org/10.1146/ANNUREV.ARPLANT.55.031903.141701

Choi, W.G., Miller, G., Wallace, I., Harper, J., Mittler, R., Gilroy, S., 2017. Orchestrating rapid long-

distance signaling in plants with Ca2+, ROS and electrical signals. Plant J. 90, 698–707. https://doi.org/10.1111/TPJ.13492

Fichman, Y., Mittler, R., 2020. Rapid systemic signaling during abiotic and biotic stresses: is the ROS wave master of all trades? Plant J. 102, 887–896. https://doi.org/10.1111/TPJ.14685

Gilroy, S., Suzuki, N., Miller, G., Choi, W.G., Toyota, M., Devireddy, A.R., Mittler, R., 2014. A tidal wave of signals: calcium and ROS at the forefront of rapid systemic signaling. Trends Plant Sci. 19, 623–630. https://doi.org/10.1016/J.TPLANTS.2014.06.013

Han, G.Z., 2019. Origin and evolution of the plant immune system. New Phytol. 222, 70–83. https://doi.org/10.1111/NPH.15596

Huang, H., Ullah, F., Zhou, D.X., Yi, M., Zhao, Y., 2019. Mechanisms of ROS regulation of plant development and stress responses. Front. Plant Sci. 10, 800. https://doi.org/10.3389/FPLS.2019.00800

Johns, S., Hagihara, T., Toyota, M., Gilroy, S., 2021. The fast and the furious: rapid long-range signaling in plants. Plant Physiol. 185, 694–706. https://doi.org/10.1093/PLPHYS/KIAA098

Källén, A., 1984. Thresholds and Travelling Waves in an Epidemic Model for Rabies. Nonlinear Anal. Theory. Methods Appl. 8, 851–856. https://doi.org/10.1016/0362-546X(84)90107-X

Källén, A., Arcuri, P., Murray, J.D., 1985. A Simple Model for the Spatial Spread and Control of Rabies. J. Theor. Biol. 116, 377–393. https://doi.org/10.1016/s0022-5193(85)80276-9

Klug, D., Rabani, J., Fridovich, I., 1972. A Direct Demonstration of the Catalytic Action of Superoxide Dismutase through the Use of Pulse Radiolysis. J. Biol. Chem. 247, 4839–4842. https://doi.org/10.1016/S0021-9258(19)44987-9

Kot, M., 2001. Elements of Mathematical Ecology, Elements of Mathematical Ecology. Cambridge University Press. https://doi.org/10.1017/CBO9780511608520

Kudryashov, N.A., 2015. Logistic function as solution of many nonlinear differential equations. Appl. Math. Model. 39, 5733–5742. https://doi.org/10.1016/J.APM.2015.01.048

Lew, T.T.S., Koman, V.B., Silmore, K.S., Seo, J.S., Gordiichuk, P., Kwak, S.Y., Park, M., Ang, M.C.Y., Khong, D.T., Lee, M.A., Chan-Park, M.B., Chua, N.H., Strano, M.S., 2020. Real-time detection of wound-induced H2O2 signalling waves in plants with optical nanosensors. Nat. Plants 6, 404–415. https://doi.org/10.1038/s41477-020-0632-4

Lew, T.T.S., Wong, M.H., Kwak, S.-Y., Sinclair, R., Koman, V.B., Strano, M.S., 2018. Rational Design Principles for the Transport and Subcellular Distribution of Nanomaterials into Plant Protoplasts. Small 14, 1802086. https://doi.org/10.1002/SMLL.201802086

Lomdahl, P.S., 1984. What Is a Soliton? Los Alamos Sci. 10, 27–31.

Mittler, R., Vanderauwera, S., Suzuki, N., Miller, G., Tognetti, V.B., Vandepoele, K., Gollery, M., Shulaev, V., Van Breusegem, F., 2011. ROS signaling: the new wave? Trends Plant Sci. 16, 300–309. https://doi.org/10.1016/J.TPLANTS.2011.03.007

Navarro, L., Dunoyer, P., Jay, F., Arnold, B., Dharmasiri, N., Estelle, M., Voinnet, O., Jones, J.D.G., 2006. A plant miRNA contributes to antibacterial resistance by repressing auxin signaling. Science (80-.). 312, 436–439. https://doi.org/10.1126/science.1126088

Petrov, V.D., Van Breusegem, F., 2012. Hydrogen peroxide—a central hub for information flow in plant cells. AoB Plants 2012, 14. https://doi.org/10.1093/AOBPLA/PLS014

Pieterse, C.M.J., Van Der Does, D., Zamioudis, C., Leon-Reyes, A., Van Wees, S.C.M., 2012. Hormonal Modulation of Plant Immunity. Annu. Rev. Cell Dev. Biol. 28, 489–521. https://doi.org/10.1146/ANNUREV-CELLBIO-092910-154055

Pinar, Z., Rezazadeh, H., Eslami, M., 2020. Generalized logistic equation method for Kerr law and dual power law Schrödinger equations. Opt. Quantum Electron. 52, 1–16.

https://doi.org/10.1007/S11082-020-02611-2

Spoel, S.H., Dong, X., 2008. Making Sense of Hormone Crosstalk during Plant Immune Responses. Cell Host Microbe 3, 348–351. https://doi.org/10.1016/J.CHOM.2008.05.009

Thaler, J.S., Humphrey, P.T., Whiteman, N.K., 2012. Evolution of jasmonate and salicylate signal crosstalk. Trends Plant Sci. 17, 260–270. https://doi.org/10.1016/J.TPLANTS.2012.02.010

Truman, W., Bennet, M.H., Kubigsteltig, I., Turnbull, C., Grant, M., 2007. Arabidopsis systemic immunity uses conserved defense signaling pathways and is mediated by jasmonates. Proc. Natl. Acad. Sci. U. S. A. 104, 1075–1080. https://doi.org/10.1073/PNAS.0605423104

Van Breusegem, F., Bailey-Serres, J., Mittler, R., 2008. Unraveling the Tapestry of Networks Involving Reactive Oxygen Species in Plants. Plant Physiol. 147, 978–984. https://doi.org/10.1104/PP.108.122325

Vega-Muñoz, I., Duran-Flores, D., Fernández-Fernández, Á.D., Heyman, J., Ritter, A., Stael, S., 2020. Breaking Bad News: Dynamic Molecular Mechanisms of Wound Response in Plants. Front. Plant Sci. 11, 1959. https://doi.org/10.3389/FPLS.2020.610445

Vestergaard, C.L., Flyvbjerg, H., Møller, I.M., 2012. Intracellular signaling by diffusion: Can waves of hydrogen peroxide transmit intracellular information in plant cells? Front. Plant Sci. 3, 295. https://doi.org/10.3389/FPLS.2012.00295

Wong, M.H., Misra, R.P., Giraldo, J.P., Kwak, S.-Y., Son, Y., Landry, M.P., Swan, J.W., Blankschtein, D., Strano, M.S., 2016. Lipid Exchange Envelope Penetration (LEEP) of Nanoparticles for Plant Engineering: A Universal Localization Mechanism. Nano Lett. 16, 1161–1172. https://doi.org/10.1021/ACS.NANOLETT.5B04467

Zandalinas, S.I., Mittler, R., 2018. ROS-induced ROS release in plant and animal cells. Free Radic. Biol. Med. 122, 21–27. https://doi.org/10.1016/J.FREERADBIOMED.2017.11.028